Experiment of Sea Breeze Convection, Aerosols, Precipitation, and Environment (ESCAPE)

Pavlos Kollias,[a,b] Greg M. McFarquhar,[c,d] Eric Bruning,[e] Paul J. DeMott,[f] Matthew R. Kumjian,[g] Paul Lawson,[h] Zachary Lebo,[d] Timothy Logan,[i] Kelly Lombardo,[g] Mariko Oue,[a] Greg Roberts,[j] Raymond A. Shaw,[k] Susan C. van den Heever,[f] Mengistu Wolde,[l] Kevin R. Barry,[f] David Bodine,[d] Roelof Bruintjes,[h] Venkatachalam Chandrasekar,[m] Andrew Dzambo,[c] Thomas C. J. Hill,[f] Michael Jensen,[b] Francesc Junyent,[m] Sonia M. Kreidenweis,[f] Katia Lamer,[b] Edward Luke,[b] Aaron Bansemer,[n] Christina McCluskey,[n] Leonid Nichman ⓘ,[l] Cuong Nguyen,[l] Ryan J. Patnaude,[f] Russell J. Perkins,[f] Heath Powers,[o] Keyvan Ranjbar,[l] Eric Roux,[l] Jeffrey Snyder,[p] Bernat P. Treserras,[q] Peisang Tsai,[n] Nathan A. Wales,[o] Cory Wolf,[n] Nithin Allwayin,[k] Ben Ascher,[f] Jason Barr,[a] Yishi Hu,[d] Yongjie Huang,[d] Miles Litzmann,[a] Zackary Mages,[a] Katherine McKeown,[g] Saurabh Patil,[d] Elise Rosky,[k] Kristofer Tuftedal,[a] Min-Duan Tzeng,[d] and Zeen Zhu[b]

ABSTRACT: Convective clouds play an important role in Earth's climate system and are a known source of extreme weather. Gaps in our understanding of convective vertical motions, microphysics, and precipitation across a full range of aerosol and meteorological regimes continue to limit our ability to predict the occurrence and intensity of these cloud systems. To improve predictability, the National Science Foundation (NSF) sponsored a large field experiment entitled "Experiment of Sea Breeze Convection, Aerosols, Precipitation, and Environment (ESCAPE)." ESCAPE took place between 30 May and 30 September 2022 in the vicinity of Houston, Texas, because this area frequently experiences isolated deep convection that interacts with the region's mesoscale circulations and its range of aerosol conditions. ESCAPE focused on collecting observations of isolated deep convection through innovative sampling and developing novel analysis techniques. This included the deployment of two research aircraft, the National Research Council of Canada Convair-580 and the Stratton Park Engineering Company Learjet, which combined conducted 24 research flights from 30 May to 17 June. On the ground, three mobile X-band radars and one mobile Doppler lidar truck equipped with soundings were deployed from 30 May to 28 June. From 1 August to 30 September 2022, a dual-polarization C-band radar was deployed and operated using a novel, multisensor agile adaptive sampling strategy to track the entire life cycle of isolated convective clouds. Analysis of the ESCAPE observations has already yielded preliminary findings on how aerosols and environmental conditions impact the convective life cycle.

SIGNIFICANCE STATEMENT: The ESCAPE field experiment provided unique observations of coastal convective cloud vertical motions, microphysics, and precipitation across a wide range of summertime aerosol and meteorological regimes. The highest aerosol concentrations occurred near the refineries in eastern Houston but did not contribute to the cloud condensation nuclei and ice-nucleating particles. The airborne measurements included frequent sampling of intense convective updraft dynamics and microphysics. A novel radar-based sampling of convective cells provided unique observations of their 3D structure throughout their life cycle. Mobile trucks equipped with soundings provided a detailed sampling of the sea-breeze structure and evolution. These datasets will be used for improving high-resolution simulations of high-impact events in coastal urbanized areas.

AFFILIATIONS: [a] Division of Atmospheric Science, Stony Brook University, State University of New York, Stony Brook, New York; [b] Environmental and Climate Sciences Department, Brookhaven National Laboratory, Upton, New York; [c] Cooperative Institute for Severe and High Impact Weather and Research Operations, Norman, Oklahoma; [d] School of Meteorology, University of Oklahoma, Norman, Oklahoma; [e] Department of Geoscience, Texas Tech University, Lubbock, Texas; [f] Department of Atmospheric Science, Colorado State University, Fort Collins, Colorado; [g] Department of Meteorology and Atmospheric Science, Penn State University, State College, Pennsylvania; [h] Stratton Park Engineering Company, Boulder, Colorado; [i] Department of Atmospheric Sciences, Texas A&M University, College Station, Texas; [j] Scripps Institution of Oceanography, University of California at San Diego, La Jolla, California; [k] Department of Physics, Michigan Technological University, Houghton, Michigan; [l] Flight Research Laboratory, National Research Council of Canada, Ottawa, Ontario, Canada; [m] Department of Electrical and Computer Engineering, Colorado State University, Fort Collins, Colorado; [n] National Center for Atmospheric Research, Boulder, Colorado; [o] Los Alamos National Laboratory, Los Alamos, New Mexico; [p] NOAA/OAR National Severe Storms Laboratory, Norman, Oklahoma; [q] Department of Atmospheric and Oceanic Sciences, McGill University, Montreal, Quebec, Canada

1. Introduction

Convective storms vertically transport water vapor and condensate from Earth's surface to the upper troposphere and, thus, in part control the global atmospheric circulation. Life on Earth is fundamentally linked to this transport, which influences the hydrological cycle and the intensity of severe weather responsible for the destruction of life and property (NASEM 2018). The scientific community continues to be confronted with knowledge gaps about convective storms that limit our predictive capabilities despite the emergence of kilometer-scale global models (Stevens et al. 2019), the advancement of artificial intelligence (AI)-based analytics (NASEM 2022), and the improvements in large-eddy simulations (LES; Gustafson et al. 2020). Characteristics such as convective core size; cloud lifetime; precipitation intensity, amount, and efficiency; and lightning flash rates are closely related to environmental factors (e.g., Igel and van den Heever 2015), as are cold pools, which are important to convective initiation and organization (van den Heever et al. 2021). Embedded in these environmental factors, aerosol loading, ranging from urban and industrial pollution sources to significantly lower background aerosol conditions over the remote oceans, could also influence cloud properties and life cycles (van den Heever and Cotton 2007; Lebo 2018; Hu et al. 2019). Adding to the challenge, convective clouds evolve rapidly, and their microphysical and kinematic properties and life cycles are challenging to resolve in observations (e.g., Fridlind et al. 2019; Ladino et al. 2017).

To methodically advance observation-based understanding of fundamental convective cloud processes and aerosol impacts on these processes, the Experiment of Sea Breeze Convection, Aerosols, Precipitation, and Environment (ESCAPE) was conducted in the summer of 2022 in the Houston area.

a. Houston's atmospheric circulation and aerosol environment. The Houston region is warm and humid in the summer and commonly experiences onshore flow and sea-breeze-forced convection (e.g., Wang et al. 2022; Tuftedal et al. 2024). These conditions frequently generate isolated convection that interacts with a range of aerosol conditions associated with Houston's urban and industrial emissions. The onshore flow also brings with it relatively clean maritime air that contrasts with the locally polluted air produced by the numerous power plants and refineries in the area.

b. ESCAPE research themes. The overarching scientific objective of ESCAPE was to collect and analyze observations of convective cloud and environmental properties to enhance the understanding of the fundamental process-level coupling between convective cloud vertical motions (kinematics), microphysics, and precipitation production across a wide range of cloud environments (including background aerosol conditions) and meteorological regimes, throughout their life cycle. Several research themes were proposed by the ESCAPE science team, including but not limited to investigations regarding the following:

- Influence of aerosol loading on cloud microphysical properties in the early cloud life cycle stage.
- Role of the complex coastal environment on convection initiation.
- Extent to which different aerosol environments promote significant differences in updraft properties.
- Role of aerosol loading, relative humidity, and land surface type on cold pool characteristics.

c. Observation-model symbiosis. One overarching challenge that has plagued previous efforts that aimed to evaluate simulated impacts of aerosols and meteorology on convective properties has been the inherent covariabilty between aerosol conditions and meteorology (Varble 2018). In general, thermodynamic and kinematic variability is expected to have a larger impact than changes in aerosol alone (Lebo 2018). A direct evaluation of modeled aerosol impacts on deep convective clouds warrants a focused field effort to constrain spatiotemporal environmental heterogeneity as well as aerosol and cloud microphysical properties over a large sample size of clouds. The ESCAPE measurements will be used symbiotically with high-resolution models to improve simulations of the life cycle of isolated convective cells to examine the effects of interactive aerosol, microphysical, and kinematic processes on observable cloud, precipitation, and electrification signatures.

2. Overview of the ESCAPE field campaign

The ESCAPE field campaign took place in Houston, Texas, from 1 June to 30 September 2022. ESCAPE overlapped with the 4-month intensive observation period (IOP) of the U.S. Department of Energy (DOE) Atmospheric Radiation Measurement (ARM)-funded Tracking Aerosol Convection Interactions Experiment (TRACER) field campaign (Jensen et al. 2022). The concurrent deployment of the DOE and NSF platforms resulted in significant leveraging and synergy in the areas of radiosonde launches, aerosol characterization, radar-based convective cell tracking, and daily forecast activities. Table 1 provides a high-level highlight of the ESCAPE campaign.

TABLE 1. ESCAPE highlights related to operations (blue) and science (green).

Three years of planning and execution during the COVID-19 pandemic

Conducted with observational platforms that were not listed in the initial proposal

Eight U.S. universities, one research center, and the NRC of Canada

Thirteen principal investigators (PIs), 15 graduate students, and 10 undergraduate students

Two research aircraft, four mobile trucks, and one C-band precipitation radar

Thirteen aircraft IOP days, 24 total flights, and 17 IOP ground days

Two forecast trials before the campaign and 60 forecast briefings (2 per day) during the campaign

Unique airborne-based characterization of aerosol conditions in the Houston area

Unprecedented sampling of intense convective updrafts dynamics and microphysics

Novel radar-based sampling of convective cells' life cycle

Detailed sampling of sea-breeze structure using mobile trucks and soundings

Other resources were used to complement the field campaign observations. These include the KHGX Next Generation Weather Radar (NEXRAD) located in the Houston–Galveston, Texas, area that can provide high-quality surveillance radar observations (including the collection of level 1 data that allows for the use of improved signal processing methods), and the Geostationary Operational Environmental Satellite (GOES) Advanced Baseline Imager (ABI) that can provide images of reflected radiation at 0.64 μm (at 0.5-km resolution) and emitted radiation at near-IR and IR channels (at 1–2-km resolution) every 5 min. Additionally, the Texas Commission on Environmental Quality (TCEQ) operates a dense surface measurement network in the region. Further, the Geostationary Lightning Mapper (GLM) aboard *GOES-16* and *GOES-17* continuously maps all lightning activity (Rudlosky and Virts 2021). The following subsections will focus on the operations and instruments that were deployed during ESCAPE.

To ensure that ESCAPE campaign objectives were met, a forecasting team and a nowcasting team were formed (Dzambo et al. 2025). Forecasting shifts comprised a mix of ~4–8 new and experienced forecasters (varying depending on staff availability) and met for around 7 h each day. Each forecaster was trained on the analysis of observations, forecast models, Hybrid Single-Particle Lagrangian Integrated Trajectory model (HYSPLIT), and thermodynamic soundings. Each forecaster was responsible for a component of the forecast, with the goal of assessing the probability, location, and timing of a shallow-to-deep convection transition along the sea breeze that was suitable for targeting by aircraft and ground-based assets. ESCAPE forecasts were tailored toward the rigid timelines and decision criteria of aircraft operations and were complemented by daily collaboration with the TRACER campaign's virtual forecasting team, situating the aircraft operations within the broader context of the large TRACER effort, thereby providing a helpful, independent, checks-and-balances-style operation.

On research flight days, the forecasting team met between 0400 and 0630 LT to confirm or refine the previous afternoon's flight plan based on the latest guidance, and a small group of forecasters from the previous day's forecasting team would join the nowcasting team to support in-flight operations by analyzing radar, satellite, and new model data in real time. Given the nature of sea-breeze-driven convection, rapidly changing environmental conditions often affected (for example) convection initiation timing; nowcasting fed back into forecasting by identifying such conditions. The team's approach resulted in nearly universally successful flight decisions, maximizing resources by ensuring the best possible conditions were observed on a given flight day and by adapting the operations plan to allow for operations in Louisiana when a persistent high-pressure ridge over Houston would have otherwise prevented all flight hours from being used. This was especially evident by the end of the campaign, where some of the most optimal sea-breeze-driven convection, as well as aerosol conditions, were correctly forecasted and measured.

Further information on the operations of forecasting and nowcasting teams during ESCAPE is found in the companion paper (Dzambo et al. 2025).

a. Airborne platforms. Two research aircraft, the National Research Council (NRC) of Canada Convair-580 and the Stratton Park Engineering Company (SPEC) Learjet conducted research flights from 31 May to 17 June. The airborne platforms included state-of-the-art remote sensing capabilities (three airborne Doppler radars and one backscatter lidar) and complete suites of in situ probes to characterize state parameters, aerosol, and cloud microphysics. In advance of ESCAPE, the science team developed flight plans for sampling the boundary layer and clouds in coordination with the aircraft pilots and air traffic control (ATC) operators in the busy Houston airspace. The flight plans were based on statistical sampling conducted with long flight legs ($\sim$60 km) and were designed to accommodate forecast input and the latest ATC guidance.

Aerosol instruments on the NRC Convair-580 measured the total aerosol concentration, aerosol size distribution, cloud condensation nuclei (CCN), and ice-nucleating particles (INPs). A mechanism was developed by NRC for inflight switching between inlet sampling in clear air and in cloud. The in-cloud residual aerosol data were collected behind a counterflow virtual impactor (CVI; Brechtel model 1204) inlet system (Shingler et al. 2012), while the clear-air aerosol was sampled behind an isokinetic inlet [Droplet Measurement Technologies (DMT), model AAA-0093]. The total concentration of aerosol particles with diameters > 0.01 μm was measured by the condensation particle counter (CPC3775; TSI Inc.). The ultra-high sensitivity aerosol spectrometer (UHSAS, DMT), a light-scattering-based instrument, collected aerosol size distributions for diameters between 0.06 and 1 μm. Two UHSAS instrument models were integrated into the NRC aircraft, namely, the UHSAS-C (cabin version, DMT) and a wing-mounted UHSAS-A (airborne, DMT).

CCN spectra were measured with three streamwise CCN counters (Roberts and Nenes 2005), comprising two miniaturized CCN counters developed at Scripps Institution of Oceanography and one CCNc-100 instrument built by DMT, supplemented with a constant pressure inlet that maintained a constant pressure of 600 hPa. CCN spectra at 0.03%, 0.41%, and 0.73% supersaturation were collected at 1 Hz. These resolved the horizontal and vertical CCN gradients in the lower troposphere (from the surface to 4 km above sea level) and along coastal—urban transects and characterized mixing between the boundary layer and free troposphere.

In situ measurements of INPs were collected using a continuous flow diffusion chamber (CFDC), installed aboard the Convair-580, like in previous studies (Barry et al. 2021). The CFDC consists of two vertically oriented temperature-controlled cylindrical walls coated with thin ice layers that condition inlet air for mixed-phase cloud activation and ice nucleation. Following droplet evaporation, the total number of INPs active at the CFDC temperature and supersaturation are detected with an optical particle counter (OPC) by distinguishing large nucleated ice particles from the small aerosol particles. During operation, the CFDC column aerosol lamina was held at constant temperatures between –33° and –20°C and supersaturations with respect to water between $\sim$3% and 7%. Filters were also collected periodically in the boundary layer using the same ambient inlet and later rinsed for processing using the Colorado State University (CSU) ice spectrometer (IS) for determination of the number of INPs in the immersion freezing mode at temperatures between approximately –28° and 0°C (McCluskey et al. 2018; Barry et al. 2021).

The Learjet primarily flew at higher altitudes than the NRC Convair-580; however, both aircraft sampled clouds in the boundary layer and in the rising turrets at higher altitudes. Some flights were designed, so cloud properties derived from measurements on the different aircraft could be compared. Particle size distributions were derived from probe

measurements on both aircrafts, including covering the complete range of cloud particle sizes, from 1 μm to >10 mm. In situ probes on the Learjet included a two-dimensional stereo (2DS) probe, a two-dimensional cloud Grey probe, a fast cloud droplet probe (FCDP), a fast forward-scattering spectrometer probe (FFSSP), and a high-volume precipitation spectrometer-4 (HVPS-4), as well as a Hawkeye, which consists of an FCDP, a 2DS probe, and a cloud particle imager (CPI). Key probes on the NRC Convair-580 included a cloud droplet probe (CDP2) and FCDP for measuring cloud droplets < 50 mm in size, a 2DS probe, and a cloud imaging probe (CIP) that provide data on particles with sizes between ~50 μm and 1 mm, and a high-volume precipitation spectrometer-3 (HVPS-3) and precipitation imaging probe (PIP) for larger particles. Data from the optical array probes were processed using the University of Illinois/Oklahoma Optical Probe Processing Software (UIOOPS; McFarquhar et al. 2018). Nevzorov and sea liquid water content (LWC) probes provided information on the bulk mass content, and a CPI and the Holographic Detector for Clouds (HOLODEC; Fugal and Shaw 2009; Spuler and Fugal 2011) provided additional information on particle images and concentrations in localized volumes.

Figure 1a shows the flight tracks of all flights flown by the NRC Convair-580 and SPEC Learjet during ESCAPE. In total, 24 research flights with a total of 92 h of flight time (60 for the Convair and 32 for the Learjet) were conducted (Table 2). Both aircraft sampled air masses over the ocean and those both east and west of Houston. In general, less-polluted conditions were measured southwest of Houston and over the Gulf of Mexico due to the clean marine air and the onshore flow. More polluted conditions were measured east of Houston, downwind of the refineries, and the Houston urban plume. Aerosol observations from CCN counters and the UHSAS were used to identify specific instances of more and less polluted conditions (e.g., pollutants from ship stacks could be sampled over the Gulf). Further, the aircraft sampled a large range of cloud growth cycles and vertical velocities. Both the air- and ground-based radar data provide context for the locations where cloud microphysical measurements were made. Combined, these data are being used to determine how convective cloud properties and evolution vary with aerosol and meteorological conditions. Ongoing efforts include statistical analyses of how cloud LWC, total cloud droplet number concentration (N_t), cloud particle size distributions (PSDs), bulk extinction (b_e), and effective radius (r_e) vary with meteorological, aerosol, and surface conditions. High-resolution modeling simulations are currently investigating the impact of different aerosol conditions on these same convective storm properties.

Unfortunately, much less convection occurred in the Houston area during the airborne phase of the ESCAPE field campaign than in any other month of the summer. The flight plans were adjusted to accommodate cloud sampling outside the Houston vicinity (Fig. 1a), including the introduction of two aerosol-focused flights and alternating statistical (long flight legs) and cloud (several passes of the same cloud) sampling. The aerosol-focused flights were instrumental in capturing some of the large variability in aerosol and CCN around the Houston area. For example, changes in aerosol and CCN concentrations of more than two orders of magnitude were measured in a dedicated research flight flown on 12 June 2022, which included relatively clean marine air from the Gulf of Mexico, spatially homogeneous conditions around Houston but with elevated super micron aerosol concentrations due to a Saharan dust transport event. Airborne observations during ESCAPE show that these contrasts in aerosol impact CCN concentrations, particularly at higher supersaturations, but not INP concentrations. The cloud sampling also resulted in an impressive dataset: hundreds of individual updrafts were sampled, with at least 75 having updraft velocity > 10 m s^{-1} and one with a maximum updraft velocity of 29 m s^{-1}. The highest liquid water contents of approximately 1 g m^{-3} were frequently found to be coincident with the strongest updrafts.
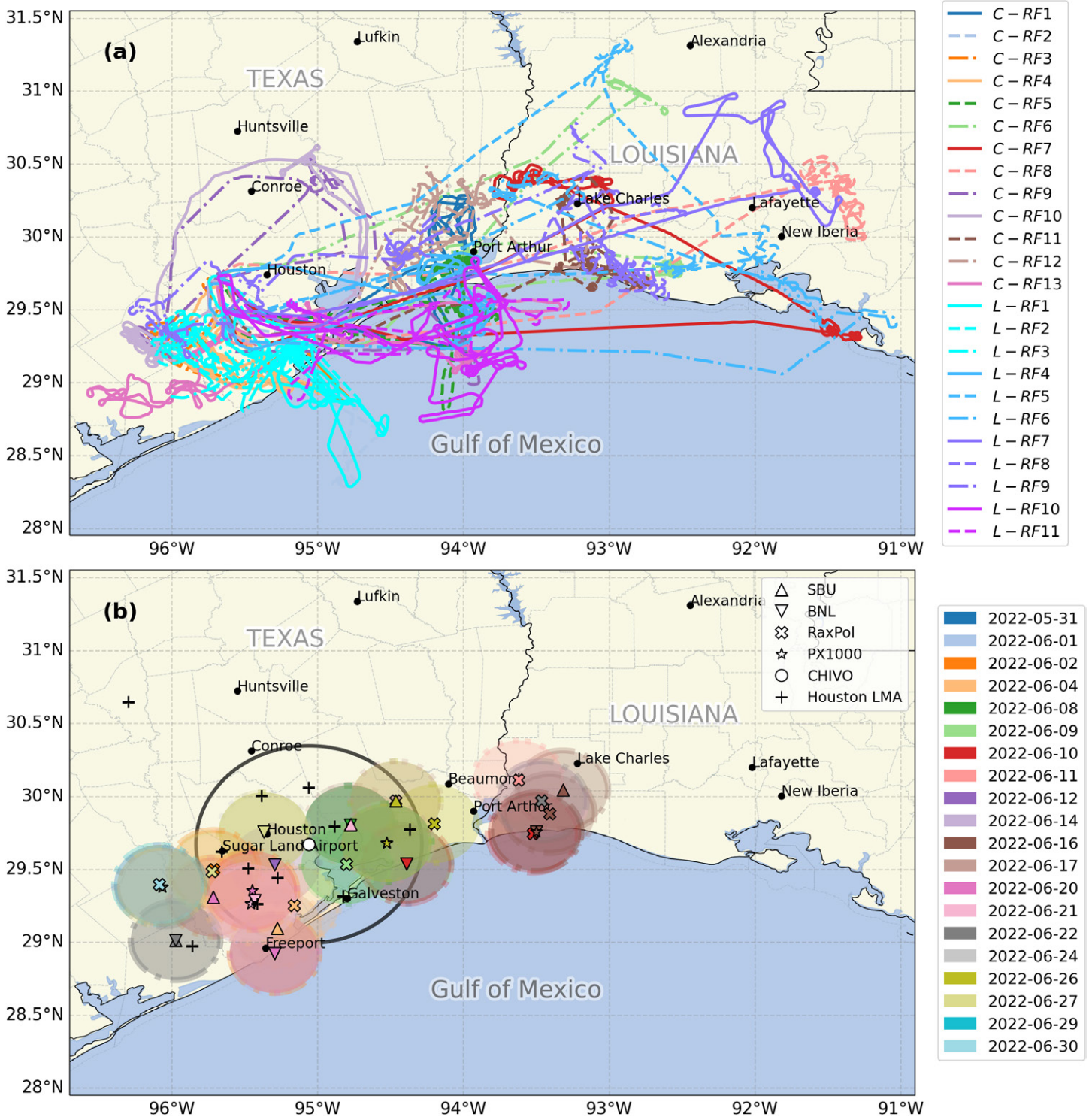
FIG. 1. (a) Flight tracks flown by NRC Convair-580 (C-RF#) and SPEC Learjet (L-RF#) during ESCAPE and (b) deployment sites for the ESCAPE ground-based mobile platforms. The shaded area indicates the 30-km radius coverage of the mobile radar trucks, and the black circle indicates the 75-km radius range of the CHIVO C-band radar. The location of the Houston LMA stations is shown with the black crosses.

b. Mobile ground-based platforms. On the ground, four mobile trucks were deployed from 30 May to 27 June, based on detailed guidance from the ESCAPE forecast team, at sites identified east and west of the Houston area (Fig. 1b). These include the rapid-scanning, X-band (3-cm wavelength), polarimetric (RaXPol), mobile radar (Pazmany et al. 2013), and the PX-1000 solid-state polarimetric X-band weather radar (Cheong et al. 2013) from the University of Oklahoma, the SKYLER-2 dual-polarization X-band phased array radar (Kollias et al. 2022a,b) from Stony Brook University and the Brookhaven National Laboratory Center for

TABLE 2. List of the ESCAPE research flights from NRC of Canada Convair-580 and the SPEC Learjet and additional (no research flight days) possible cases for the second model intercomparison project (MIP) of the Aerosol Cloud Precipitation and Climate (ACPC) initiative focused on aerosol convection interactions (ACI; Marinescu et al. 2021). Three categories of research flights (RF) are highlighted: aerosol sampling flights in Houston (blue), aerosol/cloud sampling flights in Louisiana (brown), and potential cases for the ACPC MIP (green).

Date	Convair	Lear	Conditions/area
31 May	CRF01	—	Shallow clouds with several deeper shallow convective cells with cloud-top height (CTH) over 3 km. Operations in the eastern domain.
2 Jun	CRF02	LRF01	Shallow and deep convective cells. Operations in the western domain.
	CRF03	LRF02	
4 Jun	CRF04	LRF03	Shallow and deep convective cells. Operations in the western domain.
8 Jun	CRF05	LRF04	Operations in the eastern domain both over water and over land.
9 Jun	CRF06	LRF05	Flights to Lake Charles and Lafayette (LA). Several isolated convective cells.
10 Jun	CRF07	LRF06	Sampling convection in SW LA.
11 Jun	CRF08	LRF07	Flights to Lake Charles and Lafayette (LA). Mesoscale organized convection.
12 Jun	CRF09	—	Aerosol flight around the Houston area (sample dust event).
14 Jun	CRF10	—	Aerosol flight around the Houston area (sample dust event).
16 Jun	CRF11	LRF08	Sea-breeze convection in Lake Charles (LA). Ideal conditions and ground support. Refuel in local LA airport.
	CRF12	LRF09	
17 Jun	CRF13	LRF10	Sample deep convection in Houston.
		LRF11	

Date	Radar tracking	TRACER IOP	Description of convective conditions
21 Jun	Yes	Yes	Morning development of shallow cumulus over land and later transition to deep convection.
7 Aug	Yes	Yes	Shallow cumulus over the ocean in the early morning, followed by shallow cumulus over land in the early afternoon. Deep convection developed southwest and northeast of Houston after 1700 LT.
17 Sep	Yes	Yes	Early afternoon development of deep convective cells.
18 Sep	Yes	Yes	Convective cells developed over the land in the afternoon. Polluted aerosol conditions compared to 17 Sep.

Multiscale Applied Sensing mobile observatory (Lamer et al. 2022). The SKYLER-2 and CMAS mobile trucks were equipped with radiosondes and Windsond (Markowski et al. 2018) receivers and conducted frequent balloon launches (every 30–60 min) to capture the detailed thermodynamic structure of the coastal boundary layer and its transition during the inland penetration of the sea breeze (see section 4). The CMAS truck was equipped with a profiling radar, backscatter lidar, disdrometer, meteorological station, and a Doppler lidar to provide comprehensive observations of the boundary layer during clear and cloudy conditions (Lamer et al. 2023). The ground-based platforms provided an improved description of the environment and sea breeze conditions and captured the microphysical and dynamical properties of isolated convective clouds.

c. Fixed ground-based platforms. In addition to the mobile platform, the Colorado State University C-band Hydrological Instrument for Volumetric Observation (CHIVO) radar was deployed at the ARM Mobile Facility 1 main site at the La Porte airport in Texas (29°40′78″N, 95°03′36″W) from 1 August through 30 September 2022. CHIVO was guided by the Multisensor Agile Adaptive Sampling (MAAS; Kollias et al. 2020) methodology, which leverages observations external to the "dedicated" radar (e.g., satellite and cameras) to enable the tracking of atmospheric features. Using MAAS, CHIVO tracked and sampled the entire life cycle of isolated convective cells (Lamer et al. 2023).

The extensive ground phase of the ESCAPE field campaign also exhibited flexibility in operations (Fig. 1b). Between 1 June and 30 September 2022, the MAAS framework leveraged NEXRAD surveillance data and *GOES-16* GLM to guide two C-band radars, CHIVO, and the

second-generation C-band scanning ARM precipitation radar (CSAPR-2) from the TRACER field campaign to sample over 1300 isolated convective cells. These data facilitated analyzing rapid changes of radar observables that represent the dynamical and microphysical evolution of convective cores (see section 4d) and allowed for investigating robust statistical characteristics of the cloud life cycles. Such a dataset complements volumetric analyses from the operational radar measurements and provides new insights into cell evolution.

d. The Houston Lightning Mapping Array.
The Houston Lightning Mapping Array (LMA; Logan 2021; Rison et al. 1999) detects the 3D location of the extent of lightning flashes with better than 99% efficiency over Houston. In preparation for ESCAPE and with NSF and DOE support, the permanent Houston LMA stations were supplemented with two temporary stations (south and east of Houston) that improved the detection efficiency and solution precision in those areas. The supplemental stations remained through September to support the CHIVO operations (Fig. 1b). In Louisiana, where ESCAPE extended operations took place, source detection efficiency fell ~80%, corresponding to 90%–95% flash detection efficiency (Chmielewski and Bruning 2016). Overall, August was the most active month for lightning, followed by July and September, all of which had relatively uniform spatial coverage of lightning over and in the vicinity of Houston. During the airborne phase of ESCAPE, much less lightning was observed than any other month, with a relative minimum in lightning over the longitude of Houston.

e. ESCAPE modeling.
In addition to the field experiment, the ESCAPE science plan includes a modest modeling component. The modeling objectives are twofold. One component aims to assist the daily forecasting activities by conducting automated real-time high-resolution Weather Research and Forecasting (WRF) Model simulations. Featuring a various combination of initial/boundary conditions, aerosol loadings, microphysical schemes, and planetary boundary layer (PBL) schemes, the WRF simulations were run twice daily at 0600 and 1200 UTC for the entire ESCAPE period. Eventually, more than 1600 WRF simulations were conducted, resulting in a unique large modeling ensemble database, which allows for statistically robust post-ESCAPE analysis to better understand environmental controls on convective cloud properties. This modeling practice also provides a framework for future field campaigns to supplement forecasting/nowcasting operations.

Post-campaign modeling effort will be invested to explore the role of the environment, including thermodynamics, kinematics, and aerosols, in the life cycle of convective clouds, focusing on the individual cloud cells, their propagation, as well as the timing of convection initiation, maturity, and dissipation.

The second objective focuses on understanding what controls the size, propagation speeds, depths, and intensity of cold pools and will be addressed using the Regional Atmospheric Modeling System (RAMS; Saleeby and van den Heever 2013). RAMS will be used to evaluate the control and sensitivity simulations, as well as determine whether any relationships are evident between the cold pool properties and precipitation amounts and size distributions, aerosol loading, and land surface type. The modeling results and sensitivities will be benchmarked against the comprehensive analysis and integration of all the ESCAPE measurements.

3. Research highlights
a. Aerosols.
Two research flights of the NRC Convair-580 (CRF09 and CRF10, Table 1) were dedicated to documenting the contrast in aerosol between the marine onshore flow and polluted air in the Houston metropolitan area. Figure 2a shows a time series of aerosol, CCN, and INP number concentrations during research CRF09 (12 June 2022). Total particle
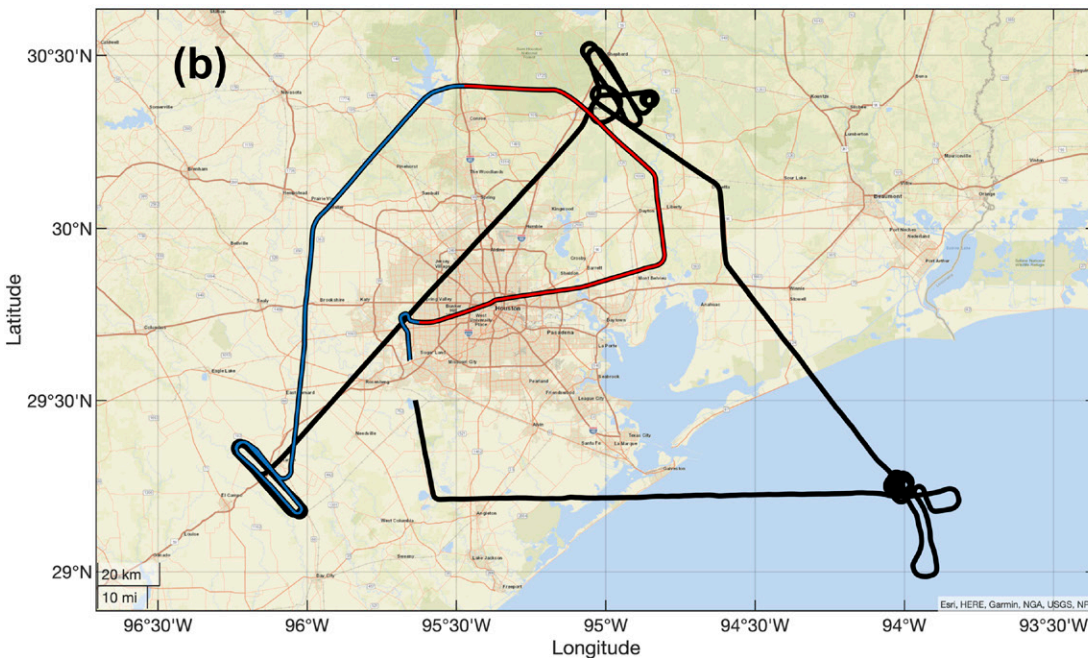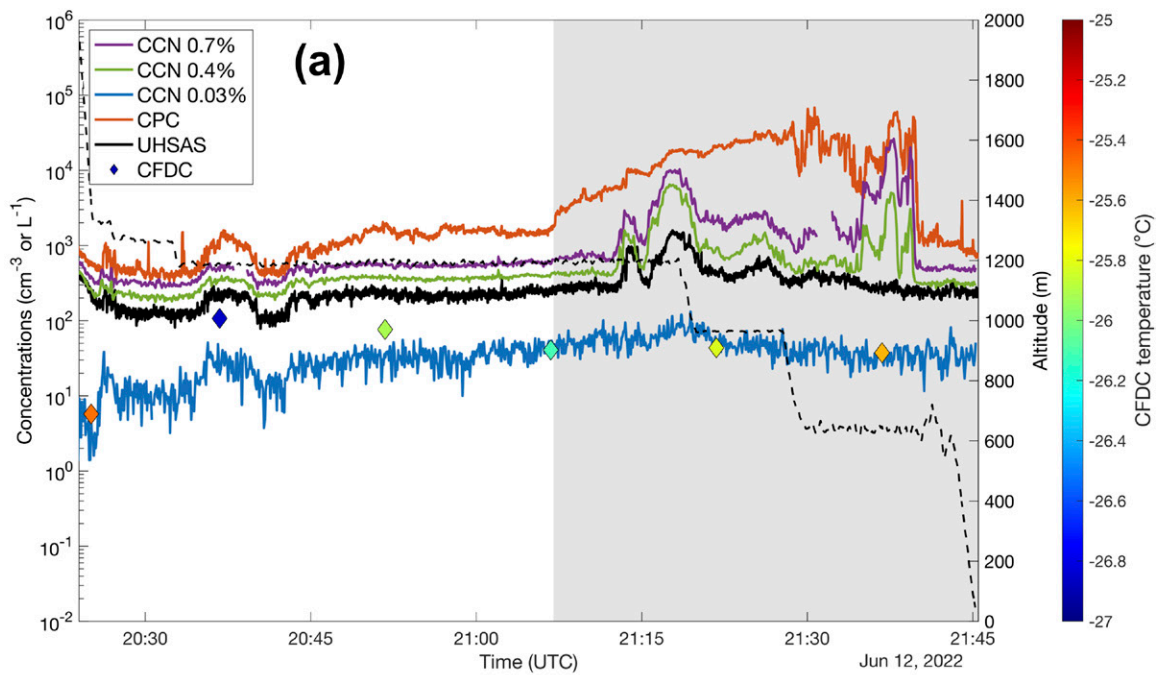
FIG. 2. (a) Time series (UTC) showing research flight circling around the Houston metropolitan area [blue and red lines in (b)]. Aerosol concentrations (CPC, $D_p > 0.01~\mu m$, and UHSAS, $D_p > 0.07~\mu m$; cm^{-3}) are shown in the red and black lines, respectively. The concentrations of CCN (0.03%, 0.41%, and 0.73% SS; cm^{-3}) are represented by the blue, green, and purple lines, respectively. INP number concentrations (L^{-1}) are indicated by the colored diamonds, where the color indicates the CFDC measurement temperature. The gray-shaded region represents the Houston plume [red line in (b)]. The altitude of the Convair-580 is shown by the dashed black line (right axis). All data are clear-air measurements. (b) Map of an aerosol research flight on 12 Jun 2022 during ESCAPE. The blue and red lines correspond to the time series shown in (a), whereas the red line here corresponds to the gray-shaded region in (a).

concentrations varied from < 500 to > 50 000 cm^{-3} while the Convair-580 flew in and out of the urban plume during a circle around Houston (Fig. 2a). During this flight, the lowest aerosol concentrations were measured southwest of Houston and represent the onshore marine air arriving from the Gulf of Mexico. Between 2045 and 2110 UTC, as the Convair-580 skirted the western edge of the Houston metropolitan area (blue line; Fig. 2b),

total particle concentrations were relatively uniform between 1000 and 2000 cm^{-3} and represented a regional urban background concentration. Aerosol concentrations increased as the Convair-580 circled around Houston, with the highest concentrations occurring near the refineries in eastern Houston (red line; Fig. 2b). The shaded gray in Fig. 2a denotes the urban plume.

The peak in CCN concentration at 2115 UTC occurred when the Convair-580 transected the urban plume downwind (and northeast) of downtown Houston. After 2130 UTC, the Convair-580 conducted a transect that flew eastward over refineries and central Houston, where total particle and CCN concentrations exceeded 50 000 and 20 000 cm^{-3}, respectively. Although changes in aerosol and CCN concentrations of orders of magnitude were observed, INP concentrations (of order 30 L^{-1} at –25° to –27°C) measured by the CFDC were consistent in and out of the Houston plume. We may note that these INP concentrations were likely influenced by the Saharan dust event occurring at the time of this flight. Using the relationship between total aerosol concentrations (CPC) and the CCN spectra, additional information about aerosol chemistry and atmospheric processes can be discerned. The peak in CCN concentrations downwind of Houston center indicates the aging of aerosols that have either grown to CCN sizes and/or their chemical composition has changed via cloud processes such that they are more hygroscopic. The airborne observations indicate that oil and gas refineries do not contribute to CCN or INPs (at least initially), whereas the highest concentrations of CCN are measured above the Houston center.

b. Cloud microphysics. NRC Convair-580 observations collected on 9 June 2022 (CRF06), when the aircraft made repeated traverses through the same cell at different temperatures, are shown in Fig. 3. The cell featured updraft speeds up to 30 m s^{-1}, in which the LWC derived from the CDP PSDs was up to 1 g m^{-3}. Examples of the size distributions and images confirm the presence of supercooled water, with the drizzle-sized drops indicating active collision–coalescence growth. A total of 271 updraft cores, defined as having vertical velocity greater than at least 1 m s^{-1} contiguously for a flight distance of at least 500 m, were sampled by the NRC Convair-580 during ESCAPE. The statistics of the convective cells tracked using the MAAS framework will also be compared with simulated convective cells tracked in LES simulations using tobac (Sokolowsky et al. 2024).

Although many of the clouds sampled during ESCAPE consisted entirely of liquid (sometimes supercooled) cloud droplets, mixed-phase clouds were also sampled, particularly the upper portions of rising turrets. The HOLODEC instrument measures the concentration and sizes of liquid droplets and ice particles simultaneously, in localized volumes, allowing for interesting opportunities to study mixed-phase microphysics (Fugal and Shaw 2009). Cloud passes in which HOLODEC measurements were not obstructed by excessive water build-up on the instrument windows were used to study the characteristics of mixed-phase cloud regions. An analysis from a flight on 16 June 2022 (CRF12) during a ~1 min cloud pass sampled from 2318:40 to 2319:30 UTC at an average temperature of –10°C is shown in Fig. 4. Panel (a) shows the number concentration N_t (cm^{-3}) of supercooled droplets along with the habits of ice particles that co-exist with the droplets. Ice habits were classified into seven different categories: short column, long column, frozen droplet, irregular, small ice, plate assemblage, and plates. The ice habit populations fluctuate throughout the cloud pass.

The local microphysical properties of cumulus clouds can vary depending on the forcing and interactions between supercooled liquid and ice. This was investigated using an algorithm developed by Allwayin et al. (2022) to identify regions of the cloud exhibiting commonly occurring but distinct PSDs. Four such regions for the supercooled droplets are identified as shown in Fig. 4b. Their relative spatial positions are marked by the shaded regions
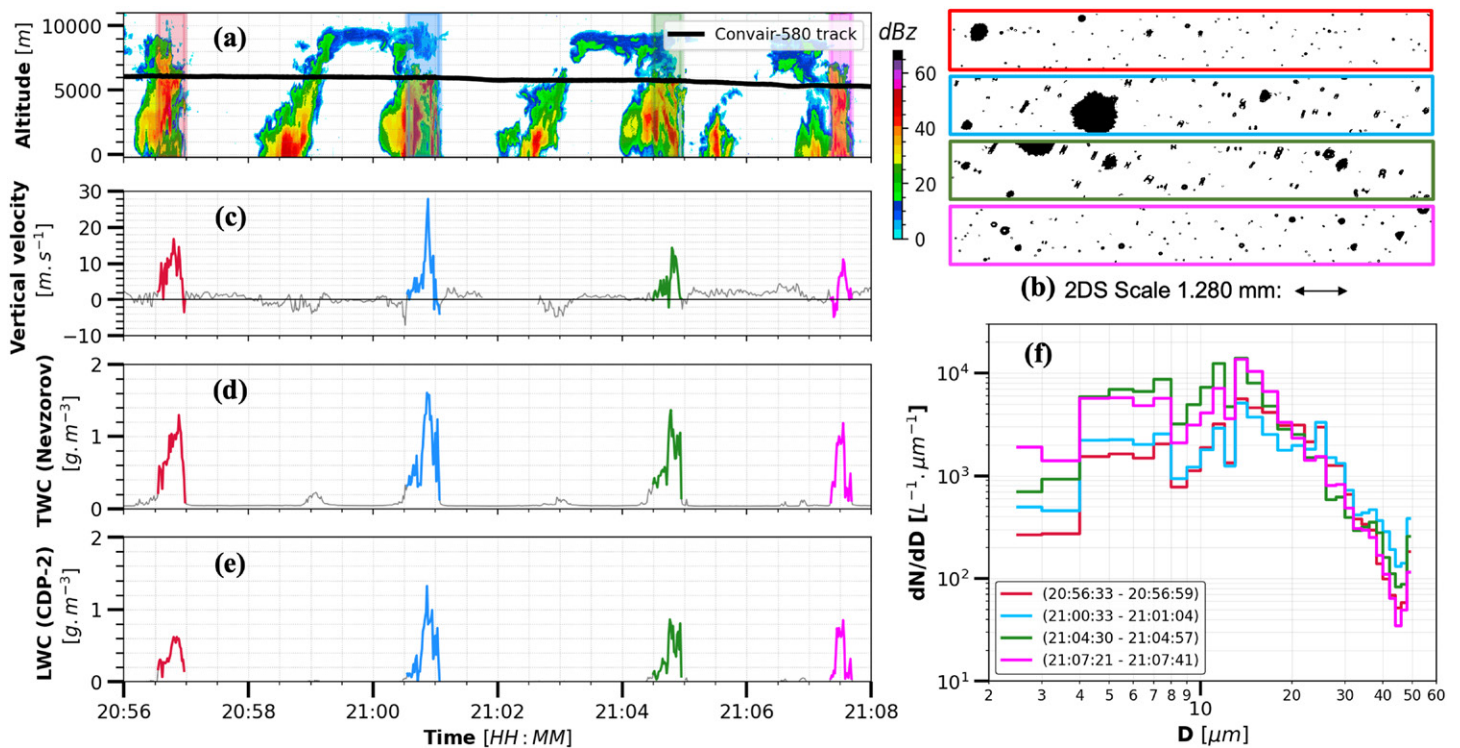
FIG. 3. Data collected using remote sensing and in situ instruments installed on the NRC Convair-580 aircraft as it made repeated passes through the same cell during CRF06 on 9 Jun 2022. (a) Vertical profile of X-band reflectivity with the altitude of the NRC Convair-580 indicated by the black line; (b) selected particles imaged by the 2DS probe at times corresponding to the colored shading in (a); (c) vertical velocity measured by the Airborne Integrated Meteorological Measurement System (AIMMS-20) probe as a function of time with updrafts as high as 30 m s^{-1} noted; (d) total water content (TWC) measured by the Nevzorov probe as a function of time; (e) LWC derived from the CDP-2 measured size distributions; and (f) particle size distributions measured by the CDP for time periods corresponding to the colored shading in (a).

(with the same colors) in the number concentration plot. Gray shading marks the region where the HOLODEC data are contaminated by precipitation accumulating on the instrument windows. Connections between the supercooled droplets and ice habits, as well as with the dynamic and thermodynamic environment, are seen. For example, the weak updraft along the edges of clouds is correlated with a characteristic PSD that has a larger mean diameter than the droplets in the middle of the cloud.

A simplified view to analyze this segment is to divide it into three main zones. First, the edge region to the left is dominated by supercooled droplets corresponding to clusters 1 and 4. The clusters have a larger mean diameter and align well near the updraft–downdraft interface at the cloud edge. The larger diameters could be explained by mixing the cloud with preprocessed air from the subsiding shell, leading to dilution by reduction of number concentrations without reducing the droplet diameters (e.g., Gerber et al. 2008; Yang et al. 2016). The right cloud edge forms the second zone and is dominated by ice crystals. This region could potentially be dominated by the Wegener–Bergeron–Findeisen process after the vapor pressure is reduced by the entrainment of dry air, making it subsaturated with respect to liquid (e.g., Korolev 2007). The cloud core forms the third region, where the cloud is mixed with two distinct clusters (clusters 2 and 3). The competition between the ice and liquid phases for water vapor could explain the smaller mean diameters of the two clusters. The results suggest the possibility that ice crystal habits are coupled to the supercooled droplets' characteristic size distributions. Future work with additional mixed-phase cloud observations is needed to further explore this possibility.

The first lightning in this cloud occurred at 2320:16 UTC (Figs. 4d,g). The Convair traveled directly underneath the flash's eventual horizontal footprint, corresponding to the period of
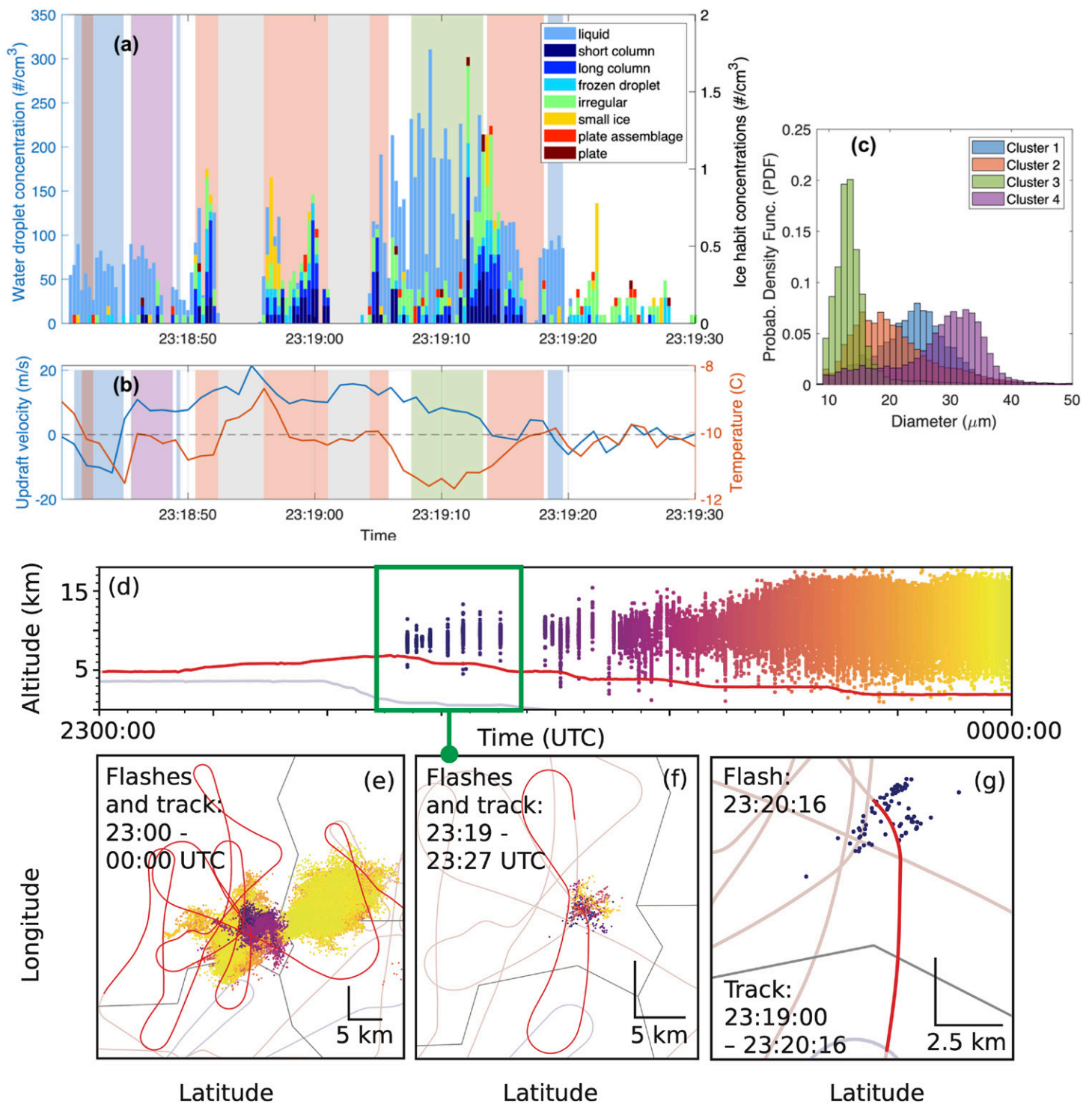
FIG. 4. (a) Supercooled liquid droplet concentration and ice habit concentrations vs time in a flight pass through a cumulus cloud during CRF12. (b) The vertical component of velocity and the temperature vs time for the same flight segment. (c) Four characteristic probability density functions for droplet diameter, as identified by a machine learning data clustering algorithm. (d) LMA time–altitude plot, with colors from purple to yellow indicating time between 2300 and 0000 UTC. The red line indicates the Convair track. (e) LMA plan view, showing the Convair track during 2300–0000 UTC (bright red) and at other times during CRF12 (light red). County borders (gray lines) and Lear tracks during other parts of the day (light blue lines) are also shown. (f) As in (e), but for LMA sources and flight tracks between 2319 and 2327 UTC, with LMA colors adjusted to that time range. (g) As in (f), but for 2319:00–2320:16 UTC; the aircraft is traveling from north to south in this panel. The green box highlights the corresponding flashes in (d) and (f).

HOLODEC observations from 2319:00 to 2319:16 UTC (Figs. 4a,b,g), when the greatest particle type diversity and maximum in droplet number concentration were observed. Thirteen more flashes happened in the same location over the next 13 min (Figs. 4d,f), followed by 42 flashes over the next 7 min (Figs. 4d,e), a sixfold jump in flash rate. After the first flash,

the Convair spiraled downward, making three more passes through the cloud (Figs. 4d,e), 1 km lower each time.

In situ validation of cloud microphysical properties in a rapidly developing thunderstorm is exceptionally rare. The particle sizes, types, and mixture of phases observed by HOLODEC illustrate the conditions expected prior to lightning in cumulus convection. The spatial variability documented in the observations provides an unprecedented opportunity for validation of coupled microphysical and electrification processes as modeled at the large eddy scale in cloud microphysics schemes (Morrison et al. 2020; Mansell and Ziegler 2013).

c. Convective cell life cycle. Individual convective cells can evolve quicker than mesoscale or synoptic-scale features. This rapid evolution has frustrated attempts to fully capture their life cycle using traditional measurements, like those obtained by NEXRAD. The TRACER and ESCAPE field campaigns achieved such sought-after observations of life cycles of individual convective storms by implementing RHI scans from two synchronized C-band scanning polarimetric radars, the CHIVO and the CSAPR-2 (Kollias et al. 2020). Using the MAAS framework, the C-band radars acquired high-resolution scans of isolated convective cells with < 30 s update times (Lamer et al. 2023; Dolan et al. 2023). In addition, when possible, the three X-band mobile radars (RaxPol, PX-1000, and SKYLER2) provided rapid-scanning volumetric observations that complement the C-band and NEXRAD radar observation.

From June to September, CSAPR-2 tracked >1000 convective cells, capturing the spectrum of convective cell life stages (Lamer et al. 2023). Figure 5a shows normalized frequency distributions of the time rate of change of maximum reflectivity through the entire convective cell (dZ_{max}/dt) estimated at each time step using the CSAPR-2 2-min cycle tracking dataset (available at https://doi.org/10.5439/1969992).

Most (96%) of the Z_{max} are found below the melting level and are associated with faster decreases in time of −5 to −2 dB min⁻¹ compared to those above the melting level, implying larger fall-out speeds for larger precipitation particles such as rain and melting graupel/hail below the melting level. Positive temporal changes include >2 dB min⁻¹ for both warm and cold phases (defined in the caption). Such rapid changes and correlations are not captured by the operational radar observations (Fig. 5a). The temporal changes in Z_{max} are well correlated with those of maximum Z_{DR} (dZ_{DRmax}/dt, Fig. 5b) and K_{DP} (not shown). Because the data samples in Fig. 5b are dominated by the warm region, the correlation suggests that positive dZ_{max}/dt represents the growth of large raindrops. A similar relationship between dZ_{max}/dt and dZ_{DRmax}/dt is also found in the cold phase, possibly representing the growth of large raindrops and producing/melting graupel particles in updraft regions. In addition to the rapid temporal changes observed, the CSAPR-2 dataset allows for the tracking of K_{DP} columns (e.g., van Lier-Walqui et al. 2016). The maximum vertical extent of K_{DP} (>2° km⁻¹) columns is well-correlated with 50-dBZ echo-top heights (Fig. 5c), especially 5–12 km in altitude, confirming the link between K_{DP} columns and updraft intensity (e.g., van Lier-Walqui et al. 2016). Above 12 km MSL, enhanced K_{DP} values are likely associated with ice crystals in the storms' anvils.

The rich microphysical information available on the convective life cycle during ESCAPE will be well-suited to causal attribution of any variations identified throughout the campaign. The case on 4 June 2022 illustrates one such opportunity when a mesoscale convective system (MCS) developed to the west of Houston along a preexisting boundary that moved into the area during the morning from the north. As the MCS propagated toward the coast, additional, short-lived, isolated cells developed to its east along the sea breeze. Lightning source rates, which roughly correspond to the number of lightning channels (Fig. 6c), are consistent with the diurnal forcing of convection by heating of the land surface, with the first cells of sufficient
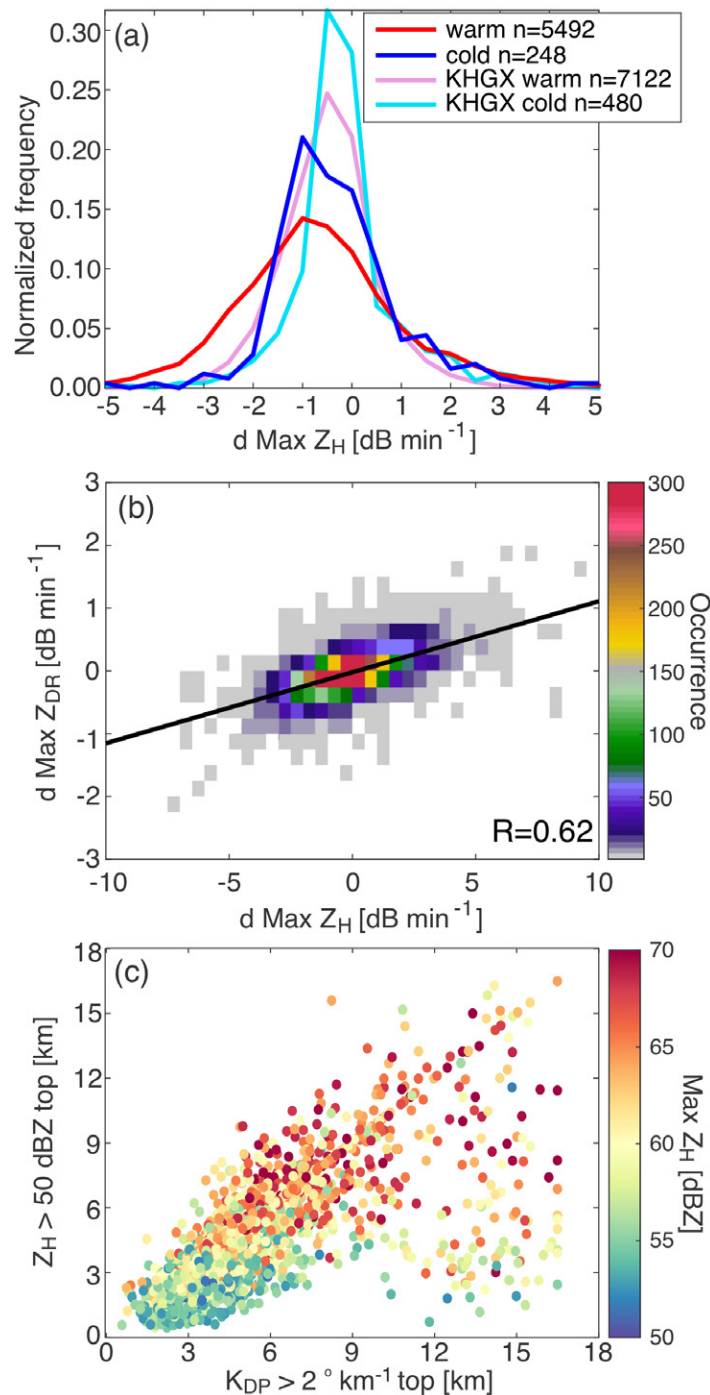
Fɪɢ. 5. (a) Frequency distributions of the temporal changes of maximum reflectivity through the convective cell columns (dZ_{max}/dt) estimated at each time step using the CSAPR-2 2-min tracking dataset (red and blue lines) and the NEXRAD KHGX dataset (pink and light blue lines) collected in the June–September 2022 period. The panel displays the frequency distribution normalized by the total number of samples for deep clouds (defined as the 30-dBZ echo-top height attained 5 km during the tracked life cycle) for the warm phase (Z_{max} observed < 4.5 km MSL, red and pink lines) and cold phase (Z_{max} observed > 5 km MSL, blue and light blue lines). The total number of samples for each profile (n) is displayed in the legend. (b) dZ_{max}/dt vs the time rate of change of maximum Z_{DR} through the convective cells (dZ_{DRmax}/dt) for all cells tracked by CSAPR-2. Color shade represents the number of samples. (c) The 50-dBZ echo-top height vs the maximum K_{DP} through the convective cell columns for all convective cells tracked by CSAPR-2. The color of the dots represents the maximum reflectivity through the convective cell columns.
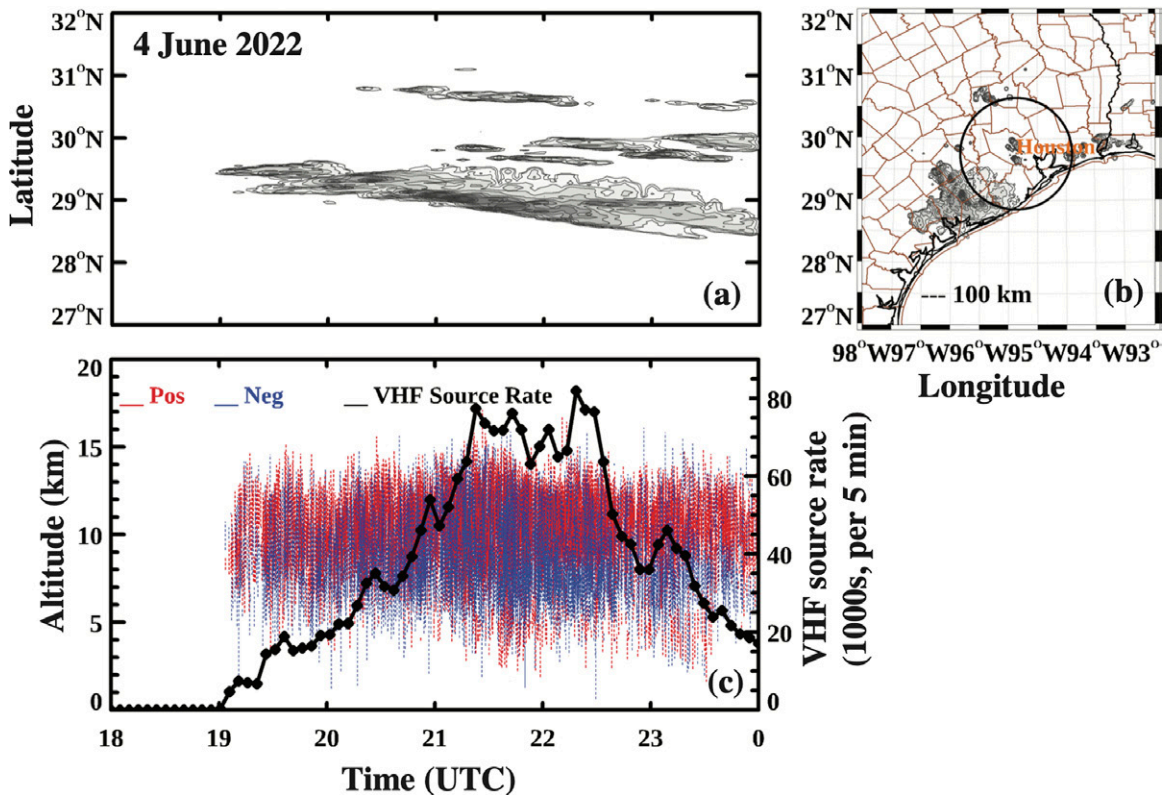
FIG. 6. LMA observations from 4 Jun 2022 for 1800–0000 UTC. (a) Relative VHF source density time–latitude Hovmoeller plot. (b) Relative VHF source density in plan view. (c) VHF source rate (black line) and VHF sources colored by charge (positive: red; negative: blue) as a function of time and altitude.

vigor to produce lightning taking place at 1900 UTC (about an hour after local solar noon) and decreasing in intensity in the few hours before sunset.

The MCS and isolated scales of convection are evident in the Hovmoeller (Fig. 6b) and plan views (Figs. 6a,b) of lightning source density. Automated charge analysis (e.g., Medina et al. 2021), which was verified by manual inspection and subsampling of individual storms, showed midlevel (6–8 km) negative storm charge between positive charge at upper (8–11 km) and lower (2–6 km) altitudes (Fig. 6c). Flashes through the lower positive charge region were relatively infrequent and often were negative cloud-to-ground strikes. This behavior is consistent with the normal tripolar structure of charge and lightning activity commonly observed in subtropical deep convection.

On the same day, the mobile radars captured the evolution of individual convective cells with unprecedented detail. Figure 7 represents height-versus-time composites of the life cycles of three convective storms observed by RaXPol PPI scans on 4 June 2022. The cells' first 40-dBZ echoes appeared at midlevels (3–6 km), followed by increased Z_H values indicating strengthening. Heavy precipitation descended to the surface, evident as "fall streaks" with average fall speeds of 8–9 m s^{-1}. Generally, large Z_{DR} values were observed just below the peak Z_H values (i.e., "leading edge" of the fall streaks), indicating raindrop size sorting (e.g., Kumjian and Ryzhkov 2012). Positive Z_{DR} extended above the environmental 0°C level for each of the cells, revealing robust Z_{DR} columns (Kumjian et al. 2014), analogous to the K_{DP} columns described above. Z_{DR} columns appeared prior to the development of larger Z_H values, suggesting increased updraft strength preceded the development of larger particles. In the first cell (~2050–2115 UTC), this fallout of heavier precipitation was also accompanied by reduced ρ_{hv} values below about 6.5 km, suggestive of liquid-coated ice particles. This was followed (~5 min later) by the maximum Z_H echo top extent growing to 9 km MSL. The Z_{DR} column reached peak height prior to the Z_H echo top reaching its maximum height,
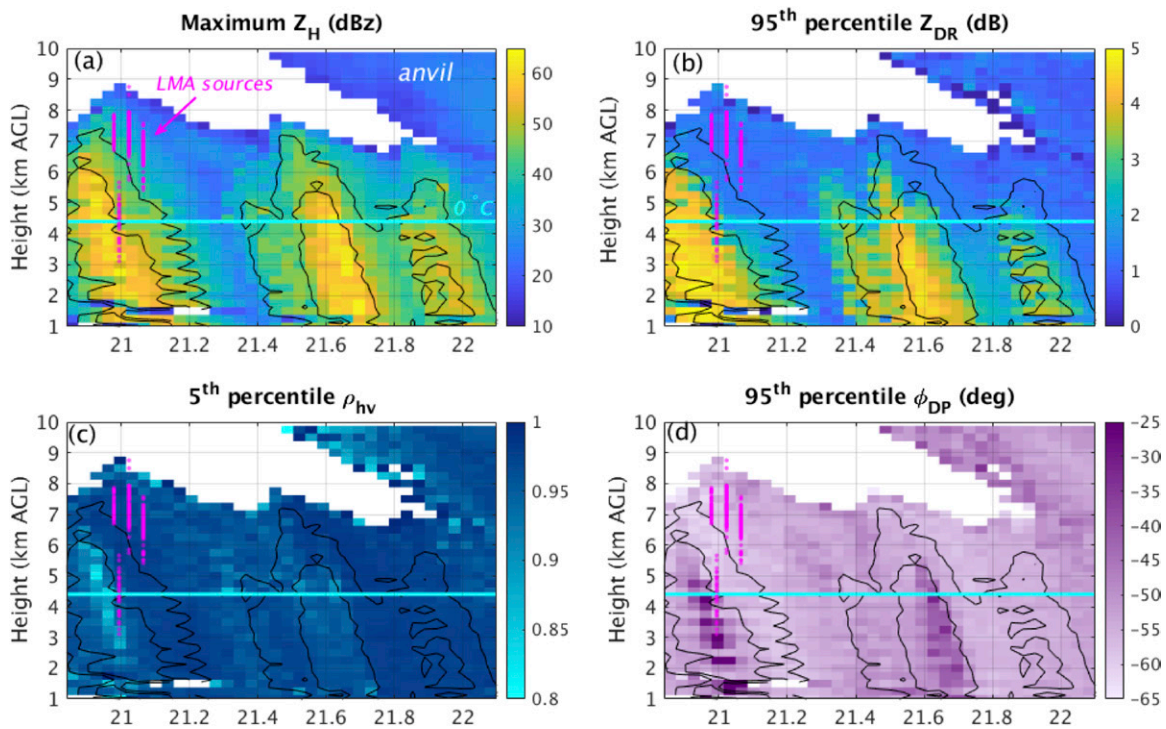
FIG. 7. Time–height depiction of three isolated convective cells derived from RaXPol volumetric data. (a) Maximum Z_H at each height level, (b) 95th percentile Z_{DR}, (c) 5th percentile ρ_{hv}, and (d) 95th percentile Φ_{DP}. In each panel, the 40- and 50-dBZ Z_H contours are overlaid. The cyan horizontal line indicates the approximate environmental 0°C level inferred from the proximity Windsond launches. Lightning sources from the Houston LMA (magenta) indicated a positive charge at the top of the cloud at about 7–8 km, a midlevel negative charge at about 5–6 km, and a lower positive charge at 3–4 km.

confirming the time lag between these updraft indicators and the better predictive value of Z_{DR} columns revealed in numerical simulations (Kumjian et al. 2014). Lightning flashes occurred (dots around 2100 UTC) after the Z_{DR} column peak height and fallout of mixed-phase hydrometeors indicated by the reduced ρ_{hv}. Similar polarimetric signals have been shown to associate with mixed-phase particle diversity known to promote charging (e.g., Bruning et al. 2007). Subsequent cells were not associated with lightning, consistent with their lower echo tops, less vertically extensive Z_{DR} columns, less mixed-phase precipitation as indicated by a smaller ϕ_{DP} signature and negligible ρ_{hv} deficits, and thus less charging. It is possible the encroaching anvil reduced the instability available to these subsequent cells (i.e., anvil shading). Therefore, although the first cell was electrified just enough to produce a few lightning flashes, later cells apparently were below that threshold. Prior to deepening, the cells that produced the two largest fall streaks were observed by the Convair (at about 3-km altitude) and Lear (at about 5-km altitude), which, together with the coordinated mobile and CSAPR-2 radar sampling of each fallstreak, will offer an opportunity for future case studies to provide detailed attribution of thermodynamic, microphysical, and aerosol contributions leading to the observed cell behavior.

d. Sea breeze and boundary layer. The spatiotemporal heterogeneities of temperature, moisture, and wind within the lower troposphere associated with convection initiation, including coastal gradients associated with the sea breeze, were characterized using Windsond and radiosonde launches from the CMAS and SKYLER2 mobile trucks. Figure 8 illustrates the vertical profiles of potential temperature (θ) for all Windsonds released during the 2 June 2022 IOP. In total, 11 sondes were launched from CMAS, located at the Surfside Beach, Texas, coastal location (located due south of Houston, Texas; Fig. 8a), and 17 sondes were launched from the SKYLER2, located at a rural inland location 56 km northwest of CMAS
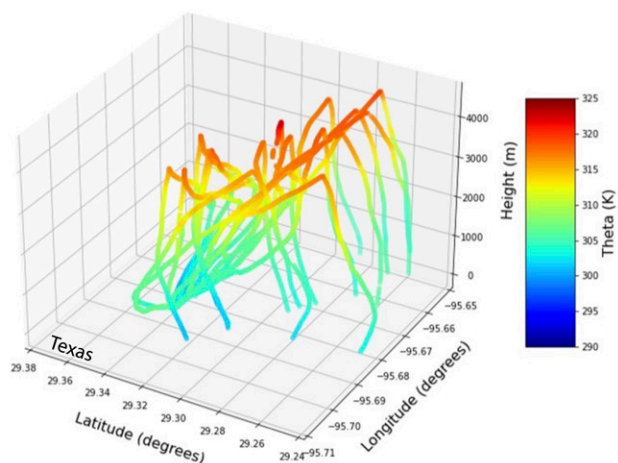
(A) 2 June 2022 CMAS Theta (3D)
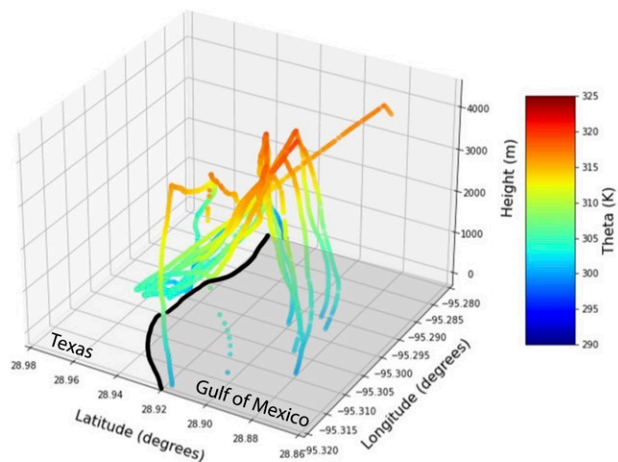
(C) 2 June 2022 CMAS Theta (2D)
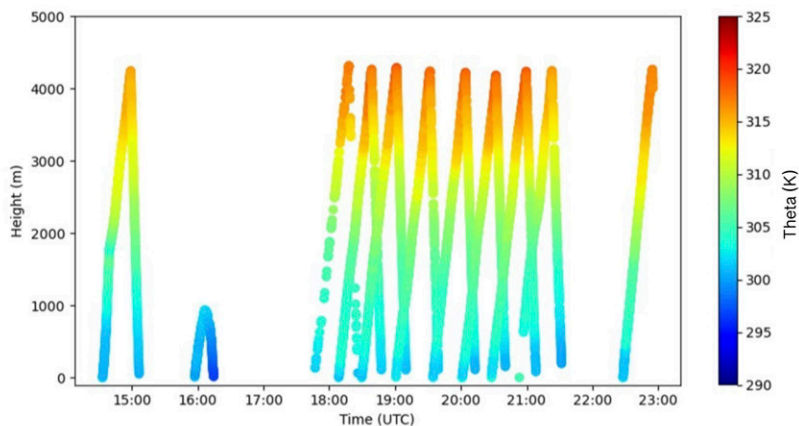
(B) 2 June 2022 SKYLER Theta (3D)
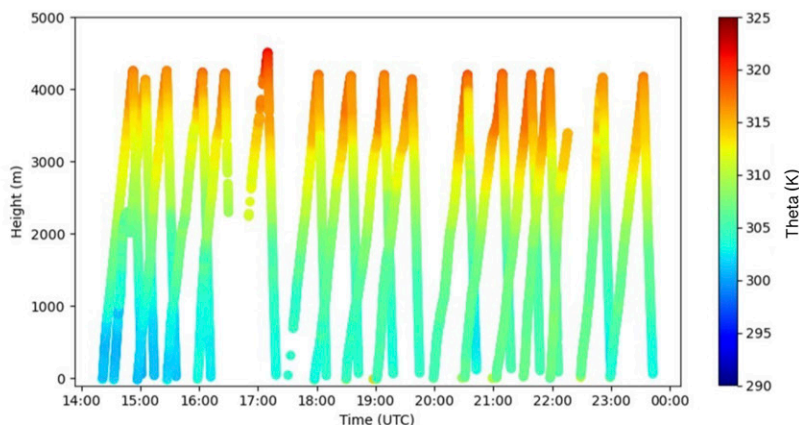
(D) 2 June 2022 SKYLER Theta (2D)

Fɪɢ. 8. **Potential temperature (K; shaded) as measured by Windsonds released during the 2 Jun 2022 IOP (a) along their 3D trajectories and (b) in time–height 2D space for all sondes released from the CMAS mobile facility. (c),(d) As in (a) and (b), but for Windsonds released from the SKYLER mobile facility. The black contour in (a) marks the location of the coastline.**

(Fig. 8b). Sondes were released between 1400 UTC (0900 LT) and 2300 UTC (1800 LT), with a target temporal frequency of 30 min and a goal of simultaneous launches from both mobile facilities (Figs. 8c,d) to observe the full evolution of the sea breeze. Data were recorded during both ascent and descent (following a controlled release of the balloons once the sondes reached 4 km in altitude). Windsonds released from CMAS landed ∼9 km south-southeast of the launch point in the Gulf of Mexico (Fig. 8a), whereas those released from SKYLER2 landed ∼7 km south-southeast of the launch point in an inland field (Fig. 8b).

The coordinated release strategy employed during ESCAPE allows the opportunity for unique spatiotemporal analyses of the lower-tropospheric coastal environment. Comparison of data gathered during the ascent of Windsonds launched at a single location (e.g., CMAS mobile facility) throughout the day provides insight into the environment's evolution, whereas comparisons of measurements from sondes released from both locations (during both ascending and descending legs) illustrate the spatiotemporal evolution of the inland–coastal horizontal heterogeneities. For example, the ascending flights of sondes launched from the CMAS coastal site recorded a 2.35 K increase in surface (sfc) −500 m vertically averaged θ between 1433 UTC (302.19 K) and 1808 UTC (303.18 K), followed by a 2.1 K decrease by 2227 UTC (Fig. 8c). In contrast, 500-m averaged θ continuously increased

throughout the day at the inland SKYLER location, from 300.27 K at 1421 UTC to 305.78 K by 2229 UTC (Fig. 8d). Thus, data suggest that the coastal CMAS location was under the influence of the marine air.

Windsond data also provide an opportunity to quantify coastal density gradients across the sea-breeze boundary, important for the movement of the sea-breeze front and properties of convective cells. Leveraging Windsond relative humidity data, sfc −500 m vertically averaged virtual potential temperature (θ_v) is calculated using data from both the upward and downward trajectories of sondes released between 2000 and 2100 UTC (not shown). Moving southward toward the coast, θ_v decreased from 308.1 K for ascending SKYLER sondes, to 307.6 K for descending SKYLER sondes, to 304.8 K for ascending CMAS sondes, and finally to 303.6 K for CMAS descending sondes. Based on these θ_v values and sonde locations, the horizontal θ_v gradient over land at this time ranged between 0.05 and 0.08 K km^{-1}, while the coast–gulf gradient (i.e., CMAS ascending vs descending sondes) was 0.15 K km^{-1}. Thus, these data indicate the presence of a diffuse density gradient over the land and a more prominent density gradient along the coast. During this event, convection initiated immediately northwest of SKYLER2, along and within the diffuse gradient inland of the coastal sea-breeze boundary.

e. Modeling activities. Preliminary analyses focused on the simulations outlined in section 2e are ongoing. Of particular interest is the large sensitivity of convection initiation and convective cloud evolution to the boundary layer scheme. An example of this sensitivity is illustrated in Figs. 9a–c for convection occurring on 16 June 2022 near the Texas/Louisiana border. Here, we compare RaXPol equivalent radar reflectivity (Fig. 9a) to model-simulated S-band reflectivity using the Mellor–Yamada–Nakanishi–Niino eddy-diffusivity mass-flux (MYNN-EDMF; Olson et al. 2019) and Yonsei University (YSU; Hong and Pan 1996) boundary layer schemes (Figs. 9b,c), all else being equal. A key structural difference between these schemes is that the MYNN-EDMF parameterization predicts both local and nonlocal fluxes in the boundary layer (the ED and MF components, respectively), while the YSU parameterization is a nonlocal scheme. The simulations conducted with the YSU scheme general initiate convection earlier and closer to the Texas/Louisiana border, exhibiting better agreement with the RaXPol observations. Note that differences in the magnitude of the reflectivity between the observations and simulations could be attributed to the different frequencies (i.e., X band vs S band).

We further compare these simulations to precipitation data from the stage IV dataset (Figs. 9d,e) across the model domain, which extends much further beyond the area captured by the radar. The trend in convection initiation is displayed here as well (Fig. 9e), with simulations conducted using the YSU scheme tending to predict precipitation earlier and with greater intensity, better matching the observations. The YSU ensemble mean predicts the precipitation maximum about 1–2 h prior to the observed peak, while the MYNN-EDMF ensemble mean is delayed by 2–4 h and with a peak magnitude that is only approximately 25% of the observed peak precipitation rate. This underprediction is related not necessarily to low precipitation rates in individual convective cells but a general misrepresentation of the location and area of convection as well as the organization of convection, as indicated in Fig. 9b compared with Fig. 9a. A statistical analysis of the simulation performance is shown in Fig. 9d, which shows the success ratio and probability of detection on the *x* and *y* axes, respectively, the critical success index (shaded) and frequency bias (dashed lines). Generally, points closer to the upper-right corner indicate better forecasting performance, i.e., values of 1 (perfect score) for all metrics. We see that the above precipitation trends between the simulations conducted with the MYNN-EDMF and YSU schemes are displayed here as improvements in all metrics (i.e., closer to 1) in the ensemble mean. Ongoing and future efforts are focused on elucidating
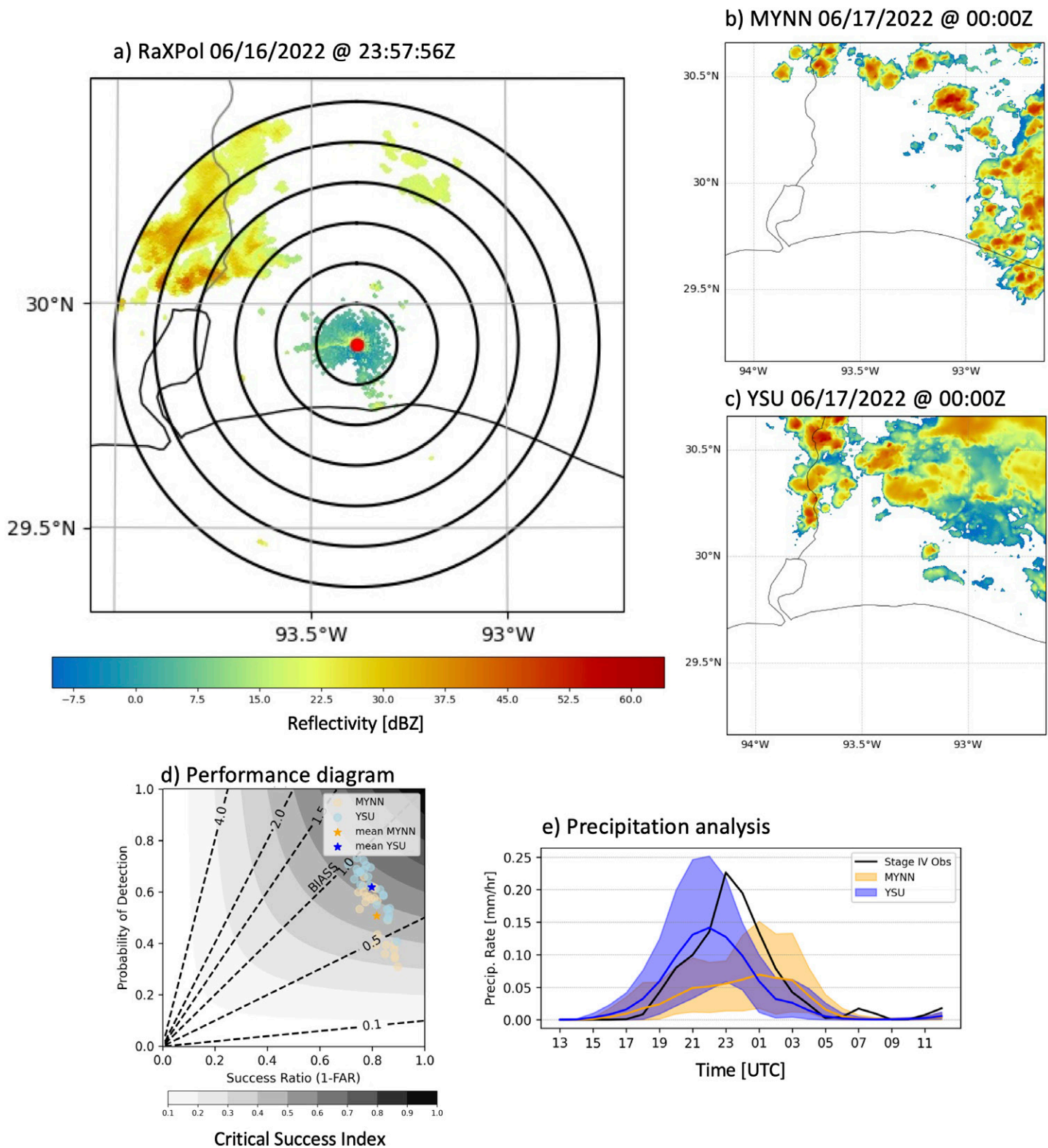
FIG. 9. Analysis of WRF ensemble for simulations initialized on 16 Jun 2022 at 1200 UTC. (a) RaXPol effective reflectivity at 2357:56 UTC. Rings denote radii at 10-km increments. Selected simulations conducted with the (b) MYNN-EDMF and (c) YSU boundary layer schemes, showing simulated S-band reflectivity at 0000 UTC on 17 Jun 2022, the nearest output time to the RaXPol data shown in (a). (d) Performance diagram for all simulations conducted with the MYNN-EDMF and YSU (orange and blue, respectively) schemes and the ensemble mean for each (dark-colored stars). (e) Comparison of precipitation rate across the model domain from the stage IV dataset (black) and the MYNN-EDMF and YSU simulations (blue and orange, respectively). For the simulations, the ensemble range is denoted by the shading, with the mean indicated by the solid-colored line.

the underlying mechanisms leading to the substantial sensitivity of convection initiation, convective cloud evolution, and precipitation to the selected boundary layer scheme.

4. Summary

ESCAPE measurements will be used symbiotically with high-resolution models to improve understanding of isolated convective cell life cycles, including the effects of interactive aerosol, microphysical, and kinematic processes on observable cloud, precipitation, and electrification signatures. The complementary observations from the ESCAPE and TRACER field campaigns are expected to provide a rich dataset on the entire life cycle of isolated convective cells and the controls of meteorology and aerosol conditions on their properties and evolution. In addition, the observations will be invaluable in upcoming TRACER and ESCAPE Model Intercomparison Project activities.

Data availability statement. All ESCAPE data are cataloged at the NCAR EOL ESCAPE data archive: https://data.eol.ucar.edu/project/ESCAPE.

SIDEBAR BOX: Discovery amid a pandemic

The ESCAPE field experiment was planned and executed during the challenging COVID-19 pandemic period. In addition to the uncertainty related to the COVID-19 pandemic, the ESCAPE team had also to manage significant changes in the NSF facilities associated with the modernization of the airborne platforms and the pool of available ground-based platforms. As a result, the ESCAPE field was conducted a year later than it was originally proposed and with a set of airborne and ground observing platforms that were not in the initial experimental design. The participation of some key observing platforms (NRC Convair-580) was secured only a couple of months before the start of the field experiment. Despite these challenges, the ESCAPE science team was able to deploy in the field the observational capabilities needed to tackle the complex nature of convective clouds with highly varying meteorological and aerosol conditions environment.

References

Allwayin, N., M. L. Larsen, A. G. Shaw, and R. A. Shaw, 2022: Automated identification of characteristic droplet size distributions in stratocumulus clouds utilizing a data clustering algorithm. *Artif. Intell. Earth Syst.*, **1**, e220003, https://doi.org/10.1175/AIES-D-22-0003.1.

Barry, K. R., and Coauthors, 2021: Observations of ice nucleating particles in the free troposphere from western US wildfires. *J. Geophys. Res. Atmos.*, **126**, e2020JD033752, https://doi.org/10.1029/2020JD033752.

Bruning, E. C., W. D. Rust, T. J. Schuur, D. R. MacGorman, P. R. Krehbiel, and W. Rison, 2007: Electrical and polarimetric radar observations of a multicell storm in TELEX. *Mon. Wea. Rev.*, **135**, 2525–2544, https://doi.org/10.1175/MWR3421.1.

Cheong, B. L., R. Kelley, R. D. Palmer, Y. Zhang, M. Yeary, and T.-Y. Yu, 2013: PX-1000: A solid-state polarimetric X-band weather radar and time–frequency multiplexed waveform for blind range mitigation. *IEEE Trans. Instrum. Meas.*, **62**, 3064–3072, https://doi.org/10.1109/TIM.2013.2270046.

Chmielewski, V. C., and E. C. Bruning, 2016: Lightning mapping array flash detection performance with variable receiver thresholds. *J. Geophys. Res. Atmos.*, **121**, 8600–8614, https://doi.org/10.1002/2016JD025159.

Dolan, B., and Coauthors, 2023: Time resolved reflectivity measurements of convective clouds. *Geophys. Res. Lett.*, **50**, e2023GL105723, https://doi.org/10.1029/2023GL105723.

Dzambo, A. M., and Coauthors, 2025: Forecasting for ESCAPE: A multi-institution hybrid forecasting and nowcasting operation for sea-breeze convection supporting a ground-based and airborne field campaign. *Bull. Amer. Meteor. Soc.*, https://doi.org/10.1175/BAMS-D-23-0015.1, in press.

Fridlind, A. M., and Coauthors, 2019: Use of polarimetric radar measurements to constrain simulated convective cell evolution: A pilot study with Lagrangian tracking. *Atmos. Meas. Tech.*, **12**, 2979–3000, https://doi.org/10.5194/amt-12-2979-2019.

Fugal, J. P., and R. A. Shaw, 2009: Cloud particle size distributions measured with an airborne digital in-line holographic instrument. *Atmos. Meas. Tech.*, **2**, 259–271, https://doi.org/10.5194/amt-2-259-2009.

Gerber, H. E., G. M. Frick, J. B. Jensen, and J. G. Hudson, 2008: Entrainment, mixing, and microphysics in trade-wind cumulus. *J. Meteor. Soc. Japan*, **86A**, 87–106, https://doi.org/10.2151/jmsj.86A.87.

Gustafson, W. I., and Coauthors, 2020: The large-eddy simulation (LES) atmospheric radiation measurement (ARM) symbiotic simulation and observation (LASSO) activity for continental shallow convection. *Bull. Amer. Meteor. Soc.*, **101**, E462–E479, https://doi.org/10.1175/BAMS-D-19-0065.1.

Hong, S., and H. Pan, 1996: Nonlocal boundary layer vertical diffusion in a medium-range forecast model. *Mon. Wea. Rev.*, **124**, 2322–2339, https://doi.org/10.1175/1520-0493(1996)124<2322:NBLVDI>2.0.CO;2.

Hu, J., and Coauthors, 2019: Polarimetric radar convective cell tracking reveals large sensitivity of cloud precipitation and electrification properties to CCN. *Atmos. Chem. Phys.*, **124**, 12 194–12 205, https://doi.org/10.1029/2019JD030857.

Igel, M. R., and S. C. van den Heever, 2015: The relative influence of environmental characteristics on tropical deep convective morphology as observed by CloudSat. *J. Geophys. Res. Atmos.*, **120**, 4304–4322, https://doi.org/10.1002/2014JD022690.

Jensen, M. P., and Coauthors, 2022: A succession of cloud, precipitation, aerosol, and air quality field experiments in the coastal urban environment. *Bull. Amer. Meteor. Soc.*, **103**, 103–105, https://doi.org/10.1175/BAMS-D-21-0104.1.

Kollias, P., and Coauthors, 2020: The ARM radar network: At the leading edge of cloud and precipitation observations. *Bull. Amer. Meteor. Soc.*, **101**, E588–E607, https://doi.org/10.1175/BAMS-D-18-0288.1.

——, E. P. Luke, K. Tuftedal, M. Dubois and E. J. Knapp, 2022a: Agile weather observations using a dual-polarization X-band phased array radar. *2022 IEEE Radar Conf. (RadarConf22)*, New York City, NY, Institute of Electrical and Electronics Engineers, 1–6, https://doi.org/10.1109/RadarConf2248738.2022.9764308.

——, and Coauthors, 2022b: Science applications of phased array radars. *Bull. Amer. Meteor. Soc.*, **103**, E2370–E2390, https://doi.org/10.1175/BAMS-D-21-0173.1.

Korolev, A., 2007: Limitations of the Wegener–Bergeron–Findeisen mechanism in the evolution of mixed-phase clouds. *J. Atmos. Sci.*, **64**, 3372–3375, https://doi.org/10.1175/JAS4035.1.

Kumjian, M. R., and A. V. Ryzhkov, 2012: The impact of size sorting on the polarimetric radar variables. *J. Atmos. Sci.*, **69**, 2042–2060, https://doi.org/10.1175/JAS-D-11-0125.1.

——, A. P. Khain, N. Benmoshe, E. Ilotoviz, A. V. Ryzhkov, and V. T. J. Phillips, 2014: The anatomy and physics of columns: Investigating a polarimetric radar signature with a spectral bin microphysics model. *J. Appl. Meteor. Climatol.*, **53**, 1820–1843, https://doi.org/10.1175/JAMC-D-13-0354.1.

Ladino, L. A., A. Korolev, I. Heckman, M. Wolde, A. M. Fridlind, and A. S. Ackerman, 2017: On the role of ice-nucleating aerosol in the formation of ice particles in tropical mesoscale convective systems. *Geophys. Res. Lett.*, **44**, 1574–1582, doi:https://doi.org/10.1002/2016GL072455.

Lamer, K., and Coauthors, 2022: Going mobile to address emerging climate equity needs in the heterogeneous urban environment. *Bull. Amer. Meteor. Soc.*, **103**, E2069–E2080, https://doi.org/10.1175/BAMS-D-21-0336.1.

——, P. Kollias, E. P. Luke, B. P. Treserras, M. Oue, and B. Dolan, 2023: Multisensor Agile Adaptive Sampling (MAAS): A methodology to collect radar observations of convective cell lifecycle. *J. Atmos. Oceanic Technol.*, **40**, 1509–1522, https://doi.org/10.1175/JTECH-D-23-0043.1.

Lebo, Z., 2018: A numerical investigation of the potential effects of aerosol-induced warming and updraft width and slope on updraft intensity in deep convective clouds. *J. Atmos. Sci.*, **75**, 535–554, https://doi.org/10.1175/JAS-D-16-0368.1.

Logan, T., 2021: An analysis of the performance of the Houston lightning mapping array during an intense period of convection during tropical storm Harvey. *J. Geophys. Res. Atmos.*, **126**, e2020JD033270, https://doi.org/10.1029/2020JD033270.

Mansell, E. R., and C. L. Ziegler, 2013: Aerosol effects on simulated storm electrification and precipitation in a two-moment bulk microphysics model. *J. Atmos. Sci.*, **70**, 2032–2050, https://doi.org/10.1175/JAS-D-12-0264.1.

Marinescu, P. J., and Coauthors, 2021: Impacts of varying concentrations of cloud condensation nuclei on deep convective cloud updrafts—A multimodel assessment. *J. Atmos. Sci.*, **78**, 1147–1172, https://doi.org/10.1175/JAS-D-20-0200.1.

Markowski, P. M., Y. P. Richardson, S. J. Richardson, and A. Petersson, 2018: Aboveground thermodynamic observations in convective storms from balloonborne probes acting as pseudo-Lagrangian drifters. *Bull. Amer. Meteor. Soc.*, **99**, 711–724, https://doi.org/10.1175/BAMS-D-17-0204.1.

McCluskey, C. S., and Coauthors, 2018: Observations of ice nucleating particles over Southern Ocean waters. *Geophys. Res. Lett.*, **45**, 11 989–11 997, https://doi.org/10.1029/2018GL079981.

McFarquhar, G. M., J. A. Finlon, D. M. Stechman, W. Wu, R. Jackson, and M. Freer, 2018: University of Illinois/Oklahoma Optical Array Probe (OAP) Processing Software. Zenodo, https://doi.org/10.5281/zenodo.1285968.

Medina, B. L., L. D. Carey, T. J. Lang, P. M. Bitzer, W. Deierling, and Y. Zhu, 2021: Characterizing charge structure in central Argentina thunderstorms during RELAMPAGO utilizing a new charge layer polarity identification method. *Earth Space Sci.*, **8**, e2021EA001803, https://doi.org/10.1029/2021EA001803.

Morrison, H., and Coauthors, 2020: Confronting the challenge of modeling cloud and precipitation microphysics. *J. Adv. Model. Earth Syst.*, **12**, e2019MS001689, https://doi.org/10.1029/2019MS001689.

NASEM, 2018: *Thriving on Our Changing Planet: A Decadal Strategy for Earth Observation from Space.* The National Academies Press, 716 pp., https://doi.org/10.17226/24938.

——, 2022: *Machine Learning and Artificial Intelligence to Advance Earth System Science: Opportunities and Challenges: Proceedings of a Workshop*. The National Academies Press, 68 pp., https://doi.org/10.17226/26566.

Olson, J. B., J. S. Kenyon, W. A. Angevine, J. M. Brown, M. Pagowski, and K. Sušelj, 2019: A description of the MYNN-EDMF scheme and the coupling to other components in WRF–ARW. NOAA Tech. Memo. OAR GSD-61, 42 pp., https://doi.org/10.25923/n9wm-be49.

Pazmany, A. L., J. B. Mead, H. B. Bluestein, J. C. Snyder, and J. B. Houser, 2013: A mobile rapid-scanning X-band polarimetric (RaXPol) Doppler radar system. *J. Atmos. Oceanic Technol.*, **30**, 1398–1413, https://doi.org/10.1175/JTECH-D-12-00166.1.

Rison, W., R. J. Thomas, P. R. Krehbiel, T. Hamlin, and J. Harlin, 1999: A GPS-based three-dimensional lightning mapping system: Initial observations in central New Mexico. *Geophys. Res. Lett.*, **26**, 3573–3576, https://doi.org/10.1029/1999GL010856.

Roberts, G. C., and A. Nenes, 2005: A continuous-flow streamwise thermal-gradient CCN chamber for atmospheric measurements. *Aerosol Sci. Technol.*, **39**, 206–221, https://doi.org/10.1080/027868290913988.

Rudlosky, S. D., and K. S. Virts, 2021: Dual geostationary lightning mapper observations. *Mon. Wea. Rev.*, **149**, 979–998, https://doi.org/10.1175/MWR-D-20-0242.1.

Saleeby, S. M., and S. C. van den Heever, 2013: Developments in the CSU-RAMS Aerosol Model: Emissions, nucleation, regeneration, deposition, and radiation. *J. Appl. Meteor. Climatol.*, **52**, 2601–2622, https://doi.org/10.1175/JAMC-D-12-0312.1.

Shingler, T., and Coauthors, 2012: Characterisation and airborne deployment of a new counterflow virtual impactor inlet. *Atmos. Meas. Tech.*, **5**, 1259–1269, https://doi.org/10.5194/amt-5-1259-2012.

Sokolowsky, G. A., and Coauthors, 2024: *tobac* v1.5: Introducing fast 3D tracking, splits and mergers, and other enhancements for identifying and analyzing meteorological phenomena. *Geosci. Model Dev.*, **17**, 5309–5330, https://doi.org/10.5194/gmd-17-5309-2024.

Spuler, S. M., and J. Fugal, 2011: Design of an in-line, digital holographic imaging system for airborne measurement of clouds. *Appl. Opt.*, **50**, 1405–1412, https://doi.org/10.1364/AO.50.001405.

Stevens, B., and Coauthors, 2019: DYAMOND: The DYnamics of the Atmospheric general circulation Modeled On Non-hydrostatic Domains. *Prog. Earth Planet. Sci.*, **6**, 61, https://doi.org/10.1186/s40645-019-0304-z.

Tuftedal, K. S., B. P. Treserras, M. Oue, and P. Kollias, 2024: Shallow- and deep-convection characteristics in the Greater Houston, Texas area using cell tracking methodology. *Atmos. Chem. Phys.*, **24**, 5637–5657, https://doi.org/10.5194/acp-24-5637-2024.

van den Heever, S. C., and W. R. Cotton, 2007: Urban aerosol impacts on downwind convective storms. *J. Appl. Meteor. Climatol.*, **46**, 828–850, https://doi.org/10.1175/JAM2492.1.

——, and Coauthors, 2021: The Colorado State University Convective CLoud Outflows and UpDrafts Experiment (C³LOUD-Ex). *Bull. Amer. Meteor. Soc.*, **102**, E1283–E1305, https://doi.org/10.1175/BAMS-D-19-0013.1.

Van Lier-Walqui, M., and Coauthors, 2016: On polarimetric radar signatures of deep convection: Columns of specific differential phase observed during MC3E. *Mon. Wea. Rev.*, **144**, 737–758, https://doi.org/10.1175/MWR-D-15-0100.1.

Varble, A., 2018: Erroneous attribution of deep convective invigoration to aerosol concentration. *J. Atmos. Sci.*, **75**, 1351–1368, https://doi.org/10.1175/JAS-D-17-0217.1.

Wang, D., and Coauthors, 2022: Linking synoptic patterns to cloud properties and local circulations over southeastern Texas. *J. Geophys. Res. Atmos.*, **127**, e2021JD035920, https://doi.org/10.1029/2021JD035920.

Yang, F., R. A. Shaw, and H. Xue, 2016: Conditions for super-adiabatic droplet growth after entrainment mixing. *Atmos. Chem. Phys.*, **16**, 9421–9433, https://doi.org/10.5194/acp-16-9421-2016.